Supporting Information: Direct Observation of Cr^{3+} 3d States in Ruby: Toward Experimental Mechanistic Evidence of Metal Chemistry

Myrtille O.J.Y. Hunault,[*,†] Yoshihisa Harada,[‡] Jun Miyawaki,[‡] Jian Wang,[¶] Andries Meijerink,[§] Frank M.F de Groot,[*,†] and Matti M. van Schooneveld[†]

†*Inorganic Chemistry and Catalysis, Debye Institute for Nanomaterials Science, Utrecht University, 3584CG Utrecht, The Netherlands*

‡*Institute for Solid State Physics, University of Tokyo, Kashiwa, Chiba 277-8581, Japan*

¶*Canadian Light Source Inc., Saskatoon, Saskatchewan S7N 2V3 Canada*

§*Condensed Matter and Interfaces, Debye Institute for Nanomaterials Science, Utrecht University, 3584CG Utrecht, The Netherland*

E-mail: m.o.j.y.hunault@uu.nl; f.m.f.degroot@uu.nl

Contents

1 Experimental results

The synthetic ruby powder was studied by scanning electron micrograph (SEM), X-ray diffraction (XRD) and AAS as described in the main text. AAS element analysis revealed 2.16 wt% of chromium. Results are shown in Figure S1.

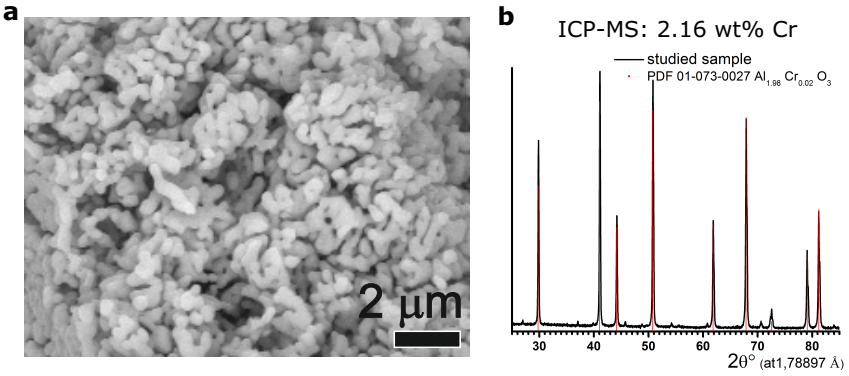

Figure S1: (a) Scanning electron micrograph and (b) X-ray powder diffractogram of the studied ruby powder. Red sticks indicate peak positions of a database match (PDF 01-073-0027) for ruby with 1 wt% of chromium.

The experimental data presented in Figure 2 are given in Figure S2 without calculations plus with an increased energy range for the RIXS spectra and RIXS spectra ***a***-***c***. We observe that the total intensity of all features follows the intensity profile of the X-ray absorption spectrum: it increases from spectrum ***a*** to spectrum ***g***, decreases for spectra ***h*** to ***k*** and increases again for spectrum ***l***. The first two RIXS features at ≈1.8 and ≈2.25 eV show the highest intensities in all spectra, as well as drastic changes in their intensity ratio for different spectra. Furthermore, the total number of observed features increases with increasing excitation energy.

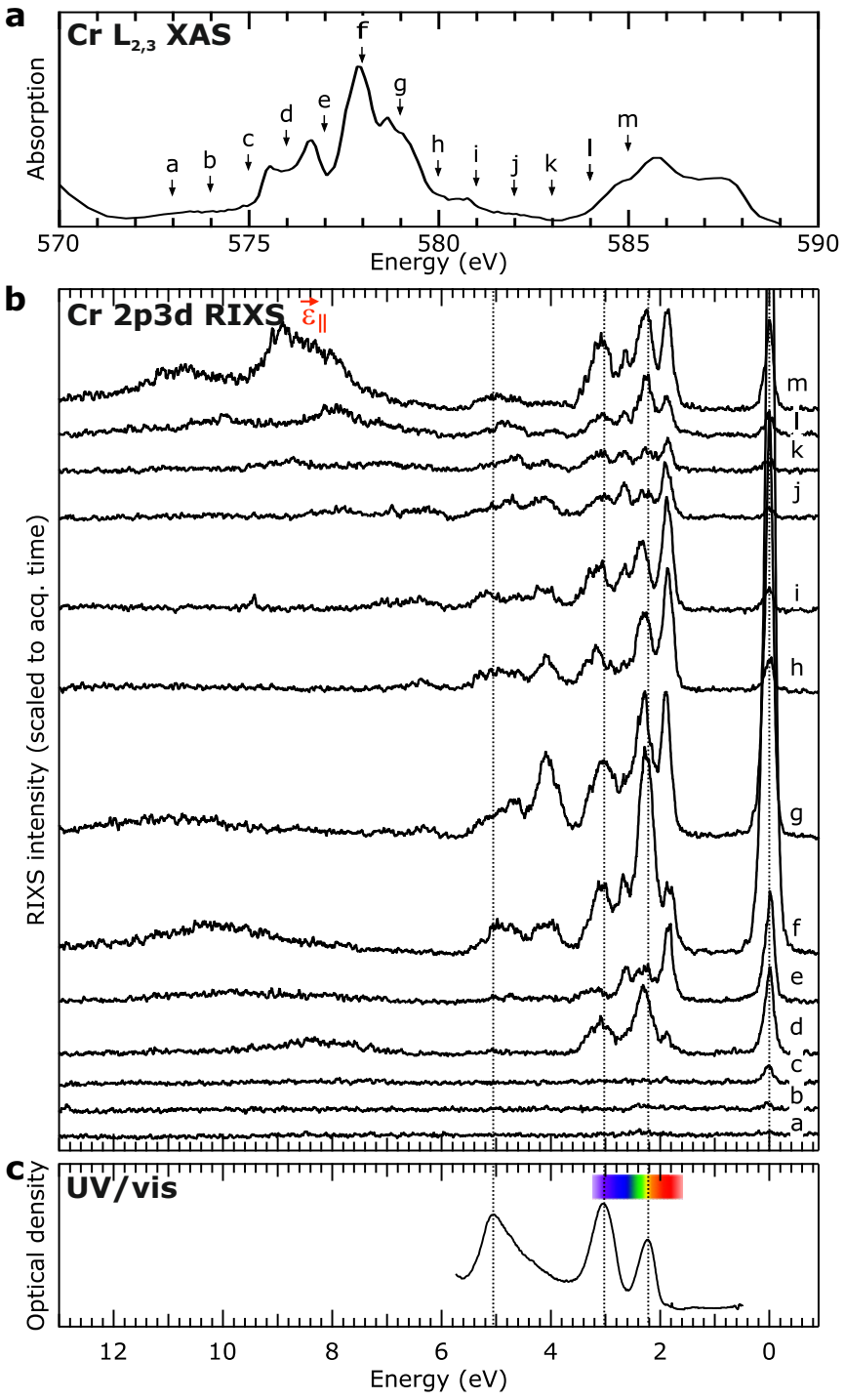

Figure S2: (a) Experimental transmission Cr $L_{2,3}$ XAS spectrum of ruby. The labeled arrows indicate the selected incident energies for the RIXS spectra shown in panel b; (b) Experimental RIXS spectra (measured in depolarized geometry $\varepsilon \parallel$). (c) Optical absorption spectrum of ruby. Colors of the visible light region have been added as an inset. The dotted lines indicate the energies of the three excited quartet states visible in UV/Vis

2 Determination of the crystal field multiplet parameters and their error

Figure S3 shows an alternative representation of Figure 2a. Here the experimental UV/Vis spectrum is used together with UV/Vis spectral calculations to obtain the effective 10Dq, Racah B and Racah C parameters of ruby. The effective 10Dq is set by the energy of the first ($^4T_{2g}$) quartet at ≈2.3 eV. With atomic F^2_{dd} and F^4_{dd} values (80% of the Hartree-Fock calculated values) the simulated blue spectrum only matches the experiment for the $^4T_{2g}$ peak. Scaling both F^k_{dd} interactions to 60% of the Hartree-Fock values (yellow calculated spectrum) yields an additional, reasonable match for the second and third quartet states ($^4T_{1g}$ at ≈3 eV and $^4T_{1g}$ at ≈5 eV), but lowers the energy of the R- and B-line doublets (sharp, 10x multiplied transitions) to too low values. By increasing F^4_{dd} back to 80% (gray calculated spectrum) both the doublets and quartets match the experimental spectrum well. The error in the derivation of these parameters is very small (below 5%) since any other set of values using a three-parameter (10Dq, F^2_{dd} and F^4_{dd}) model will give significant deviations of the calculated spectrum from the experiment.

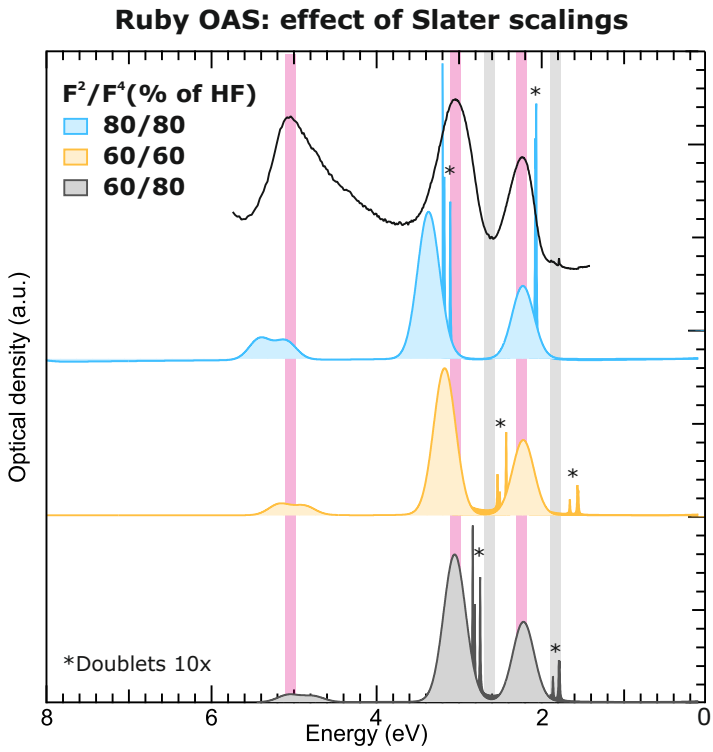

Figure S3: Experimental (black; top) and calculated UV/Vis spectrum used to determine the crystal field and Coulomb electron-electron interactions.

Figure S4 shows a similar approach to Figure S3, but now for the XAS spectra. Here the relative scaling of the G^1_{pd} and G^3_{pd} Slater parameters, accounting for electron exchange interactions, is determined. Although the improved match of the XAS calculated spectral shape with the experiment is strongest as a result of unequal F^2_{dd} and F^4_{dd} scaling, a small additional improvement is found by scaling G^1_{pd} and G^3_{pd} in similar unequal ways.

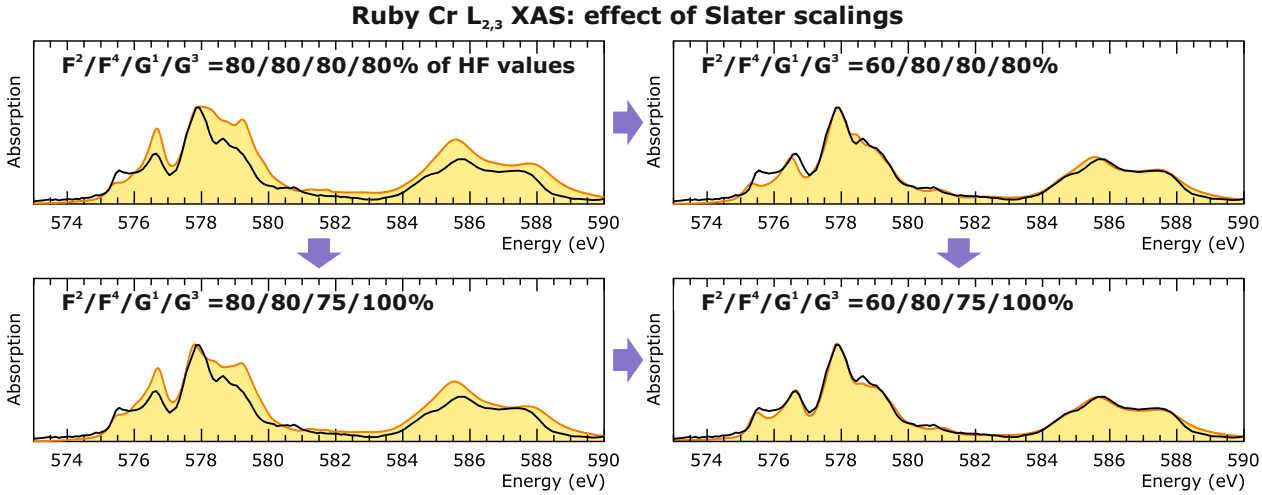

Figure S4: (a) Experimental (black) and calculated (yellow) $L_{2,3}$ XAS spectra used to determine additional exchange G_{pd} electron-electron interactions in the core-hole excited $2p^5 3d^6$ state.

Within the crystal field multiplet model, the intensely studied electronic structure of Cr^{3+} in ruby helps significantly in the restriction of a number of parameters. For example, the C_{3v} point group parameters $D\sigma$ and $D\tau$ of the Cr^{3+} site were dictated by two aspects. First, the experimental splitting of the $^4T_{2g}$ and $^4T_{1g}$ (O_h) multiplet states in $^4A_1$, or $^4A_2$, plus ^4E states is known. Sugano and Tanabe reported splittings of ≈60 meV (500 cm^{-1}) to result from the C_3 site distortion.[S1] These splittings, further discussed in Figure S5 are observed in peak broadenings in both RIXS and isotropic OAS data, and cause the polarization dependence of the OAS spectra as discussed in Figure S6. Second, the chosen C_{3v} symmetry splits the R-lines according to the experiment. Note here that, the 3d spin-orbit coupling parameter ζ_{3d} was set to 17.5 meV (≈50% of its atomic value), in-line with its value of 140

cm^{-1} derived by Sugano and Tanabe[S1] from optical absorption and electron paramagnetic resonance observations. Figure S5 shows energy-level diagrams of the Cr^{3+} $3d^3$ electron states (at 10Dq = 2.32 eV, Racah B = 0.071 eV and Racah C =0.429 eV as established for ruby in the main text) as a function of the C_{3v} trigonal crystal field parameters Dσ and Dτ. The left panel shows the variation in Dτ at zero Dσ, while the middle panel shows the variation of the levels as a function of Dσ at zero Dτ. The middle panel discloses (see purple ellipse) that Dσ is not able to significantly split the energies of the $^4A_2$ and ^4E quartet states stemming from the $^4T_{1g}(^4F)$ quartet in O_h symmetry. The left panel reveals that only for negative Dτ values the $^4A_2$ state is higher in energy than the ^4E state (see purple ellipse). From optical polarization data[S2] (see also the inset in Figure S6a) and the polarization-dependent selection rules given in the final section of the Supporting Information, it follows that this condition is met in ruby. From the actual value of the splitting being 60-100 meV[S1–S3] the Dτ value is finally determined to be -0.012 eV (indicated by purple, vertical guideline in the left panel). Subsequently, in the last panel Dσ is varied again but now at the determined Dτ value. For the splitting of the remaining two quartets (the $^4T_{2g}(^4F)$ and $^4T_{1g}(^4P)$) under influence of the trigonal distortion, it is also known that that the $^4A_1/^4A_2$ states possess higher energies than the ^4E states.[S2,S4] Furthermore, the exact energies of the R-lines are measured in the UV/Vis spectra. Both resulting conditions are met (as indicated by the purple ellipses and line) at a Dσ value of -0.057 eV.

Figure S6a contains an inset reproduced from Fairbank et al. (Figure 2 in Ref. S2) showing the light polarization-dependence of optical absorption spectra on a ruby single crystal. For reasons of clarity the original figure has been mirrored against a vertical axis. The first two main absorption bands from the right are highlighted in gray and yellow to enhance visibility. The gray (yellow) enhanced spectrum is the one taken with the electric field component of the light perpendicular (parallel) to the C_3 axis of the crystal. The lowest energy feature is the first feature from the right, hence the $^4T_{2g}(^4F)$ (O_h) manifold. The second peak is the $^4T_{1g}(^4F)$ (O_h) manifold. Our calculations using the V_{pd} hybridization

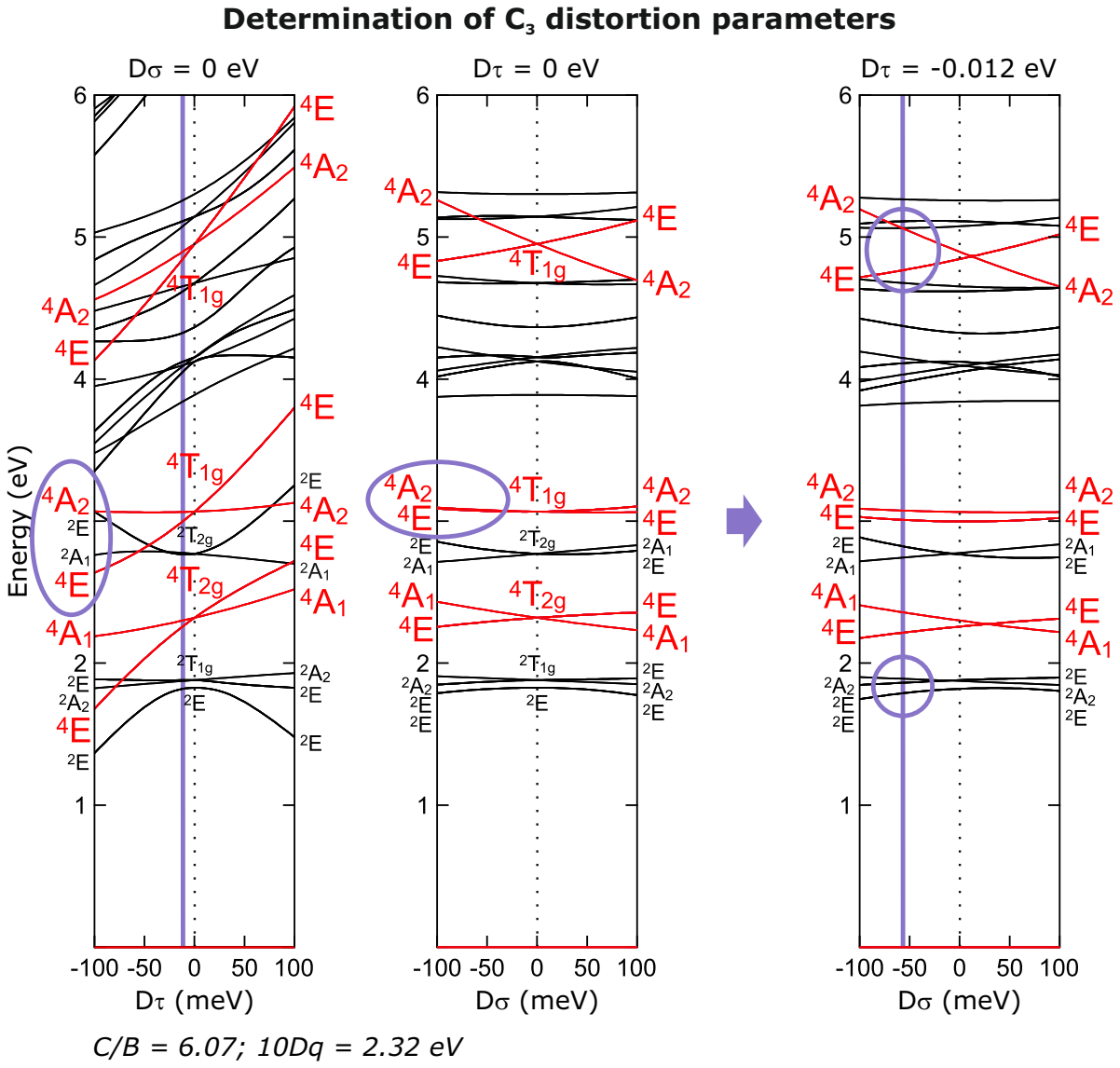

Figure S5: Energy-level diagrams used to obtain the C_{3v} symmetry crystal field parameters Dτ and Dσ in ruby. Scans of the state phase behavior as function of Dτ at Dσ = 0 eV (left), of Dσ at Dτ = 0 eV (middle) and of Dσ at Dτ = -0.012 eV (right) yield Dτ = -0.012 eV and Dσ = -0.057 eV. Purple lines and ellipses highlight essential parts in value determination (see upporting text). At Dσ = Dτ = 0 eV spectroscopic terms are labeled in O_h symmetry, else they are labeled in C_{3v} symmetry.

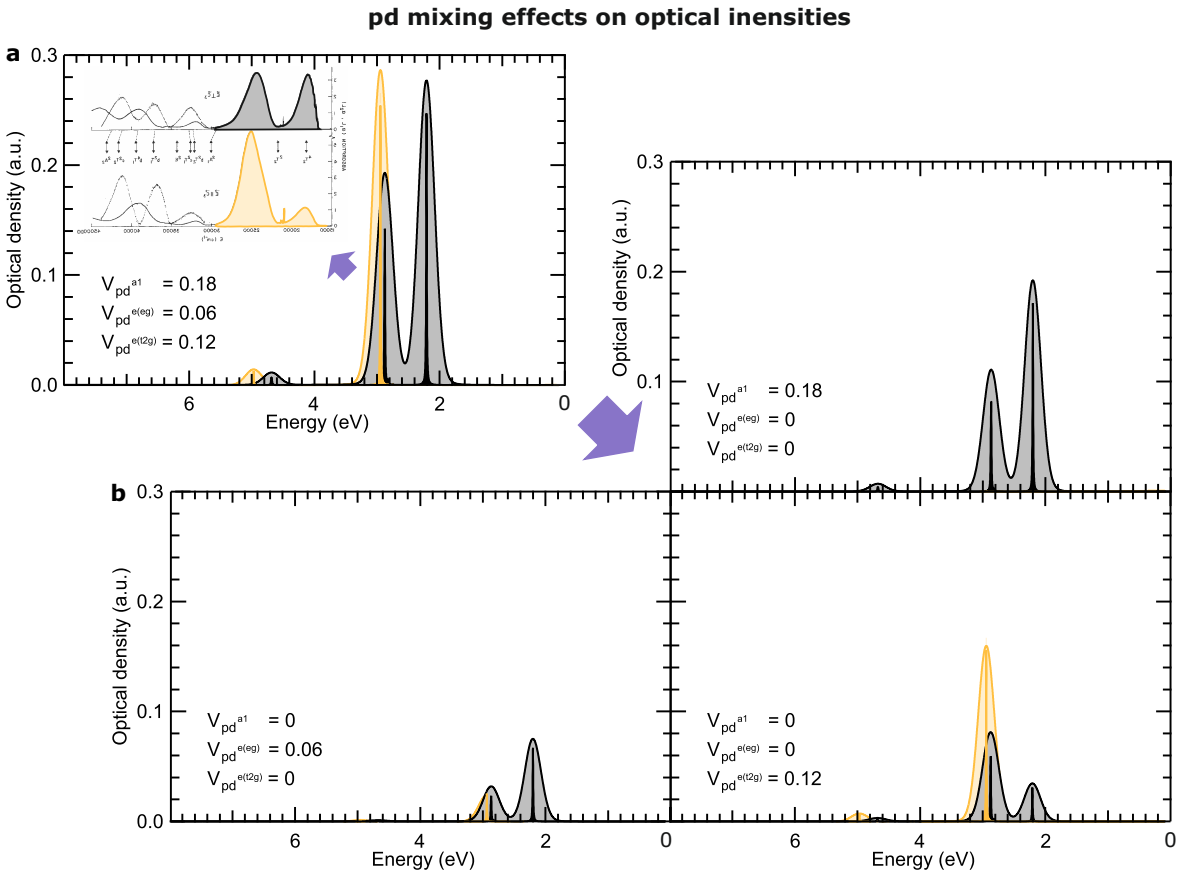

Figure S6: Intensities of the calculated optical absorption spectra explained. (a) Calculated dichroic spectra with polarization parallel (yellow) or perpendicular (gray) to the C_3 axis and compared to experimental data acquired on a ruby single crystal (inset; reproduced from ref. S2; first two transitions highlighted). (b) Total intensities in (a) are a result of orbital $p-d$ mixing strengths of 0.18 eV for A_1 states (top; right), 0.12 eV for E' states (bottom; right) and 0.06 eV for E" states (bottom; left).

potentials as indicated in Figure S6a reproduce the dichroic data from Fairbank's experiment (inset). Both the relative intensities, plus the energy shift of the maximum of the $^4T_{1g}$ feature to higher energies in the $\vec{E} \parallel C_3$ w.r.t. the $\vec{E} \perp C_3$ case, are reproduced. Figure S6a shows simulated optical absorption spectra when individual V_{pd} hybridization potentials for the A_1, E' and E" symmetries are considered. The sum of these individual contributions is not exactly equal to the spectrum in Figure S6a, because of cross-terms (interferences) affecting the intensities of the contributions when simulated all together. We observe that the $^4A_2$ (C_{3v}), arising from the splitting of the $^4T_{1g}(^4F)$ (O_h) manifold, can only be reached by electric dipole transitions from the $^4A_2$ (C_{3v}) ground state of $3d^3$ when $\vec{E} \parallel C_3$ (see the appendix of the Supporting Information). The manifold gains intensity from the E-symmetry term of the hybridization Hamiltonian. The $^4A_1$ (C_{3v}) arising from the splitting of the $^4T_{2g}(^4F)$ (O_h) manifold is never reached whatever the hybridization, because of the selection rules for electric dipole transitions. However, according to Fairbank's data, a weak transition is observed which can be attributed to further static and dynamic mixing of states enabled by the lower, but real C_3 (thus not C_{3v}) point group symmetry of the Cr^{3+} site in ruby.

3 RIXS polarization and temperature effects

As mentioned in the main text, the derived CFM parameter set also allows the correct calculation of low temperature (35 K) and polarized RIXS spectra. The experimental polarization dependence of the RIXS spectra taken at excitation energies ***f*-*j*** at low (top panel) and room temperature (middle panel) are shown in Figure S7a. The low temperature data suffer from poor statistics, however we do not observe any significant differences between the spectra taken at low and room temperature for both polarizations. This is highlighted in Figure S7b, were the low and room temperature depolarized experimental RIXS spectra are overlaid. There is hardly any difference observed between the two data sets. This does not come as a surprise since the ground state manifold is $^4A_2$ (in C_{3v}) and only consists of four microstates, which further split under influence of 3d spin-orbit coupling forming two Kramers doublets. With a spin-orbit coupling value of 17.5 meV, the splitting is $\approx 10^{-5}$ eV and as a result, the first four microstates are equally populated at 35K and RT according to a Boltzmann distribution. In the bottom panel of Figure S7a the calculated polarization dependence is shown.

Concerning the polarization behavior, the experiment exhibits a significantly higher intensity of the elastic peak (at 0 eV) for the polarized spectra compared to the depolarized spectra. This behavior is well reproduced by the simulations in agreement with selection-rules (see Section 6). According to Matsubara et al., the selection rules of the 2p3d RIXS process imply that for the ground state $^4A_{2g}$ (in O_h), the allowed final state symmetries are: A_{2g}, E_g, T_{1g}, and T_{2g} for the polarized configuration, and T_{1g} plus T_{2g} for the depolarized light.[S5] Since the final state of the elastic peak is the same as the ground state, the selection rules would predict a null intensity of the elastic line for the depolarized configuration. In the C_{3v} point group, the allowed final state symmetries for the polarized configuration are A_1, A_2, and E. For the depolarized case the allowed final state symmetry is E. This predicts that similarly to the O_h case, the elastic line should have a null intensity in the depolarized case in C_{3v} . The polarization-dependence of the elastic line intensity is also predicted identically

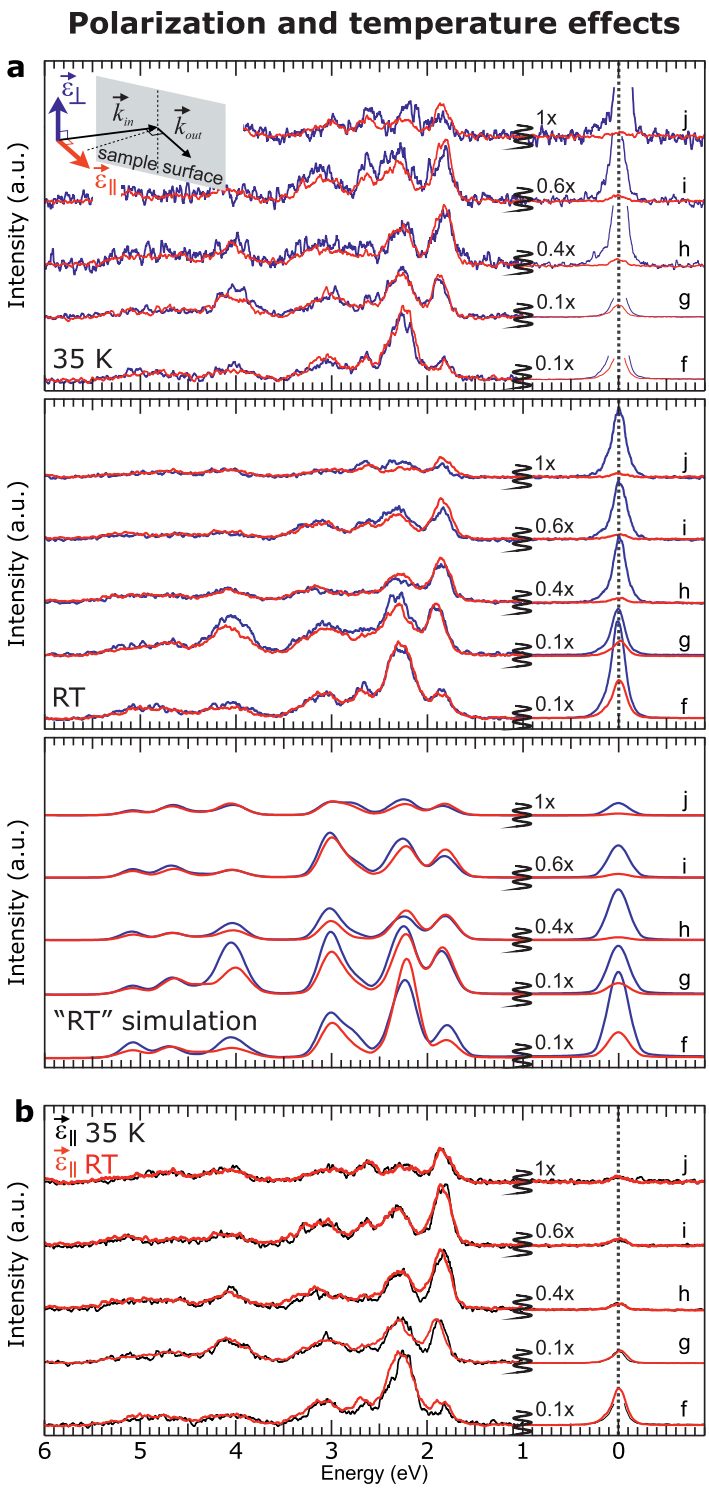

Figure S7: (a) Polarized (blue) and depolarized (red) experimental RIXS data at 35 K (top) and room temperature (middle), together with calculated RIXS spectra (bottom) for excitation energies ***f*-*j***. The inset in the top panel depicts the light polarization configurations. (b) Overlay of the 35 K and room temperature experimental depolarized data.

for the C_3 point group. The experimentally observed deviation from the null intensity in the depolarized case is therefore not a result from the point group symmetry, but is claimed to be an effect of spin-orbit coupling.[S5] The well-known, experimentally observed weak (strong) intensity of the elastic line intensity in depolarized (polarized) spectra can however not be only explained by considering these selection rules. Instead, in Figure S12 we proof that interference effects in the RIXS intermediate state play a crucial role in the polarization dependent behavior of the elastic line.

The d-d excitations seen as inelastic features (> 0 eV) in the RIXS spectra also show a polarization dependence. The dependence is relatively small, since according to the selection rules cited above, only transitions to A_{2g} and E_g symmetry levels (in O_h) should present polarization dependence. Polarization dependence is also predicted in C_{3v} and C_3 subgroups. The small polarization effects are evidenced in the experimental data. In the calculated spectra, differences due to polarization are relatively larger, nevertheless for almost all peaks in Figure S7 the trends in enhancement or decrease of RIXS intensities as a function of polarization are well reproduced.

4 Where to best measure the 3d o-DOS with RIXS, why and what to do with it

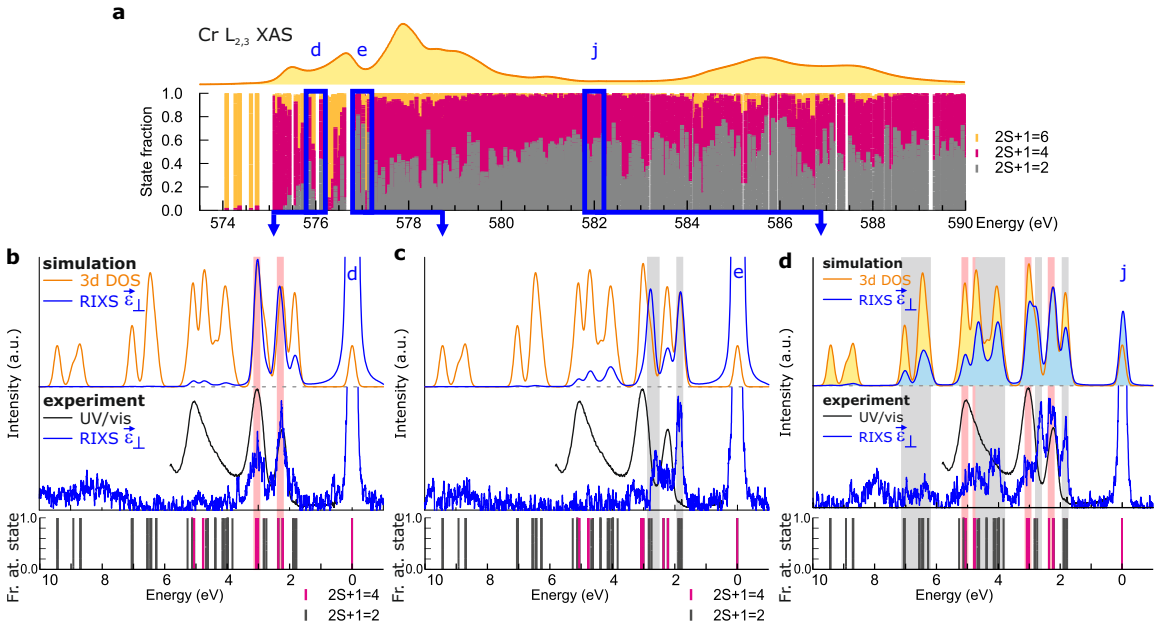

Figure S8: (a) Analysis of the spin-multiplicity of all electronic states forming the displayed Cr $L_{2,3}$ XAS spectrum. The labels ***d***, ***e*** and ***j*** refer to the excitation energies of the RIXS spectra given in Figure 2. (b) Top: the calculated, excited-state 3d optical density-of-states (o-DOS; orange line) of ruby together with the calculated polarized RIXS spectrum at energy ***d*** (blue line). Middle: the experimental UV/Vis (black line) and polarized RIXS spectrum at ***d*** (blue line). Bottom: spin-multiplicity analysis of all electronic states in the $3d^3$ ground state of ruby. (c) Analogous results to those in panel b, but now with the RIXS spectra at energy ***e***, and (d) at energy ***j***. Pink/grey bands in panels (b-d) indicate quartet/doublet states visible in the RIXS experiment. The legend in (b) applies equally to (c-d).

In Figure S8a the simulated XAS spectrum is shown together with the spin-multiplicity analysis under it (the same as Figure 3a of the main text). In Figure 3b-3d the polarized RIXS spectra at excitation energies ***d***, ***e*** and ***j*** are shown. In Figure 4a we explained that polarized RIXS at excitation energy j, measures a large part of the total excited 3d o-DOS. We repeat here that this can be seen from the high degree of overlap between the blue, calculated RIXS line at ***j*** and the calculated, orange 3d o-DOS curve in the top of panel Figure S8d. In Figures S8b and S8c it is seen that the overlap between the calculated RIXS

spectra at these energies and the 3d o-DOS curves is significantly less. Figures S8b and S8c are complementary to Figure 3 of the main text in which the selectivity for states with a certain spin-multiplicity was shown for depolarized RIXS slices ***d*** and ***e*** . That selectivity holds equally for the polarized RIXS spectra as shown from the calculated and experimental RIXS spectra in those panels.

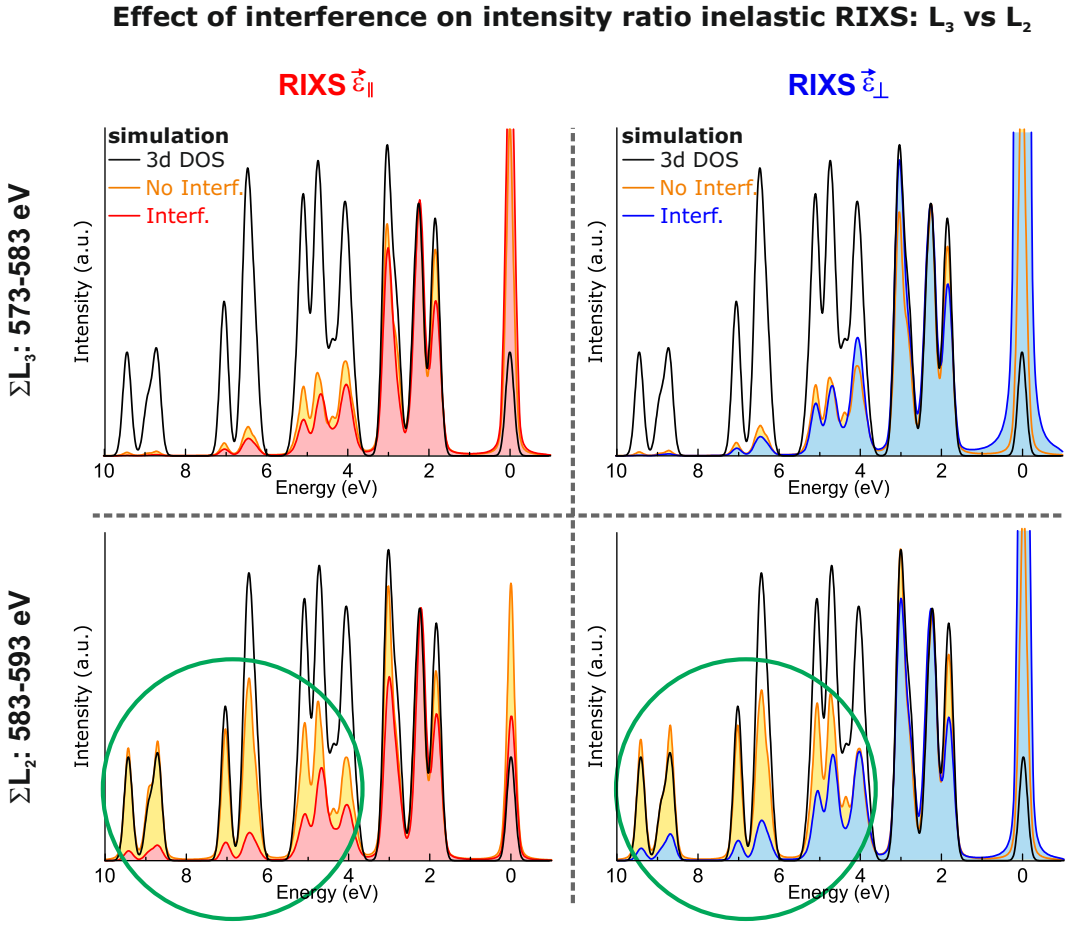

Figure S9: Calculated depolarized (left) and polarized (right) RIXS spectra with (red/blue) and without (yellow) Kramers-Heizenberg interference, summed over the full L_3 (top) or L_2 (bottom) XAS edge. The calculated, excited-state 3d o-DOS is given by a black solid line in all panels. The spectra are normalized in a way not to exceed the o-DOS curve, as to compare the relative intensity profiles of the RIXS spectra to that of the o-DOS. Green circles refer to regions of interest as discussed in the text.

While in Figure S8 the comparison between the 3d o-DOS and RIXS spectra was only

shown for three energies, Figure S9 shows comparisons between the 3d o-DOS and RIXS calculated spectra summed over the full L_3 (E=573-583 eV) or L_2 (E=583-593 eV) XAS edge. Note that it is now the black curve that represents the 3d o-DOS of the system, while the orange curve gives the RIXS calculations without interference effects in the RIXS process. This means that the calculations without interference do not follow the Kramers-Heisenberg formula that formally describes RIXS, but instead treat the X-ray absorption and subsequent X-ray emission steps as two separate processes that do not interfere with each other (which is not the case in RIXS). The comparison between the RIXS calculations with and without interference effects, teaches which part of the 3d o-DOS in RIXS spectra is not visible as a result of the RIXS interference. The top, left panel of Figure S9 shows that the relative intensities of the inelastic features of depolarized RIXS spectra, summed over the XAS L_3 edge, are hardly influenced by interference effects. The top, right panel shows that the same holds for the polarized RIXS data. The bottom, left panel of the Figure, shows however that interference effects decrease the relative intensities of high-energy d-d states drastically, for the spectra summed over the L_2 XAS edge. Similar behavior is exhibited by the polarized RIXS spectra. These results imply that it does not help significantly to measure at higher energies than excitation energy ***j*** (582 eV), if one wants to measure as much of the 3d o-DOS as possible with RIXS. At high excitation energies in the XAS edge, interference effects are large, which limits the number of observed d-states to similar numbers and intensities that can be seen in the inter L-edge region. While one advantage of measuring as many possible d-states by exciting on top of the L_2 XAS edge would be that the overall signal intensity per time will be larger, at least two complicating issues would arise: (1) measuring in the XAS L_2 edge might result in d-state intensity ratios that significantly differ from the 3d o-DOS, because of a larger variation in contributions of states with different spin-multiplicities (as in the inter-L edge range see Figure S8a); (2) the XAS L_2 edge contains additional (super) Koster-Cronig Auger decay channels that might affect the RIXS spectral shape, and which are not accounted for in most calculations. Figure S9 and the above arguments, are the

reason that one can measure and understand most of the 3d-states at an (or close to an) excitation energy in the inter L-edge region, such as energy $\boldsymbol{j}$ in our study.

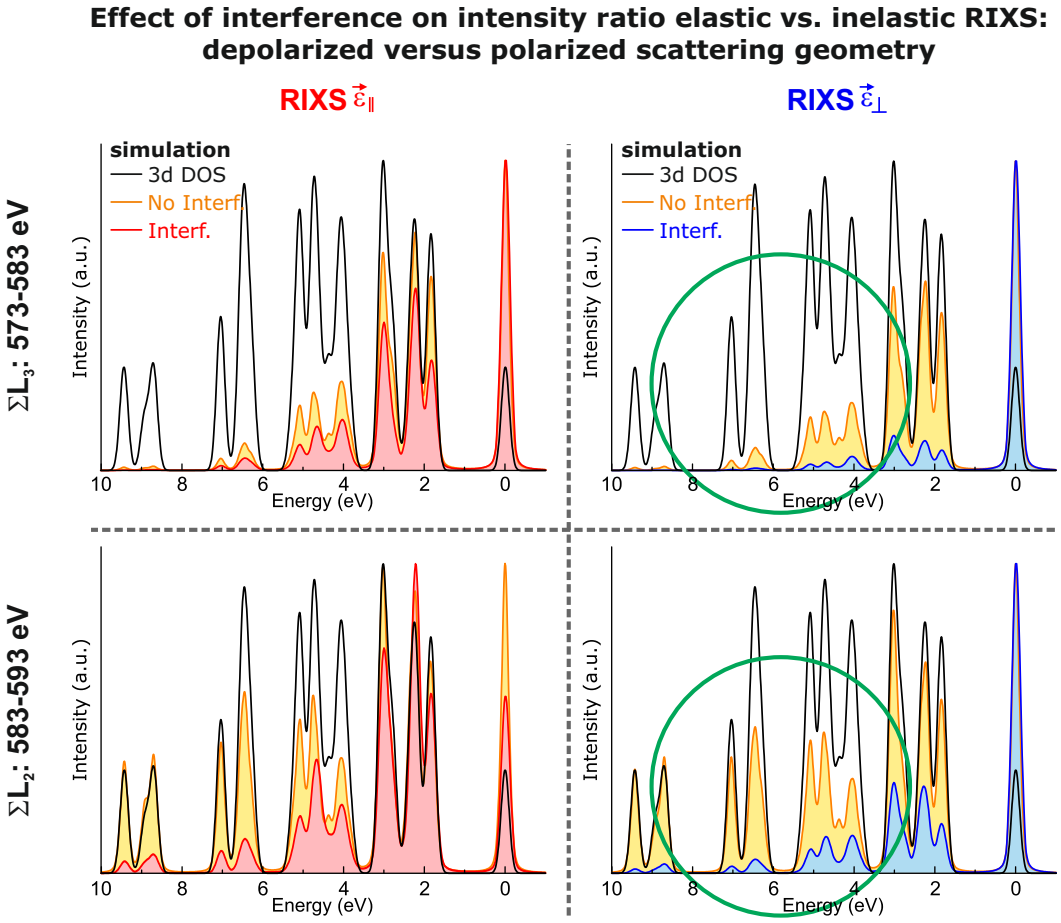

Figure S10: Calculated depolarized (left) and polarized (right) RIXS spectra with (red/blue) and without (yellow) KH interference, summed over the full L_3 (top) or L_2 (bottom) XAS edge. The calculated, excited-state 3d o-DOS is given by a black solid line in all panels. The spectra/o-DOS are normalized to unity, as to highlight the relative intensity profile of the elastic line compared to the inelastic features of the RIXS spectra under the different circumstances. Green circles refer to regions of interest as discussed in the text.

Figure S10 contains the same calculations as Figure S9, but the RIXS spectra are now scaled to unity to accentuate the relative intensities of the elastic RIXS feature (at 0 eV) versus the inelastic features (>0 eV). The top, left panel shows that the overall relative intensity ratio between the elastic and inelastic RIXS features is hardly influenced by interference

effects in the depolarized spectra summed over the L_3 XAS edge. The top, right panel reveals that for the polarized RIXS spectra, summed over the same energy range, this behavior is very different: the intensity of the inelastic features becomes significantly smaller compared to the elastic peak when interference effects are included. For the depolarized (bottom, left panel) and polarized (bottom, right panel) spectra summed over the L_2 XAS edge the results are identical. Hence, the well-known, typical elastic peak intensity behavior as a function of linear polarization (depolarized small/equal intensity compared to inelastic features; polarized large intensity compared to inelastic features) is in fact not a selection rule-only effect as previously suggested,[S5] but a combined selection rule plus RIXS interference effect.

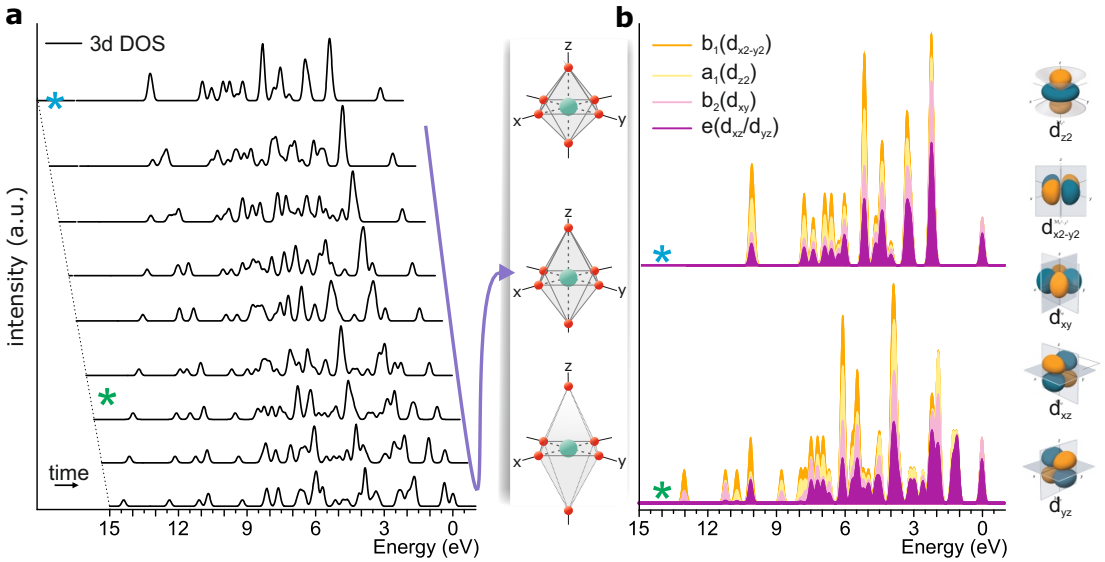

Figure S11: (a) Simulated evolution of the Cr^{3+} 3d o-DOS upon removal of the two axial ligands of a perfect octahedral, six-fold coordinated ion. An ionic representation of the change is given to the right. (b) 3d orbital decomposition of each 3d o-DOS state for the case of a Cr^{3+} ion in perfect octahedral symmetry (top; position in (a) indicated with a blue asterisk) and at the point at which the axial ligand to metal bonds are considered to be broken (bottom; position in (a) indicated with a green asterisk).

Figure S11a shows the evolution of the 3d o-DOS of a Cr^{3+} ion, surrounded by six octahedral ligands, during the removal of the two axial ligands (drawn to the right). The intensity profiles change significantly as a result of the changing ligand geometry and this

behavior will be largely measurable as shown in Figure 4a of the main text. Naturally this requires RIXS measurements on the time-scale of the chemical transformation, which should be possible with the femtosecond resolution available at the X-ray free electron lasers (e.g. European XFEL, SwissFEL, LCLS, etcetera). Figure S11b shows the contributions from the individual 3d orbitals to each 3d state. The color representations are cumulative (as in the main text) and the top panel shows the 3d o-DOS of the perfect Cr^{3+}-O_6 octahedron, while the bottom 3d o-DOS is the one where the two axial ligands are formally dissociated from the metal ion (D_{4h} point group). Note: in Figure 4b of the main text the crystal field of the tetrahedron was chosen to be -4/9*10Dq, with 10Dq being 2.24 eV for the O_h case. The crystal field of the square plane was chosen such that in a one-electron description $3d_{xz/yz}$, $3d_{z^2}$, $3d_{xy}$ and $3d_{x^2-y^2}$ orbitals have their energies at -5.1Dq,-4.3Dq, 2.3Dq and 12.3Dq, respectively (10Dq = 2.24 eV, Ds = 0.77 eV and Dt = 0.13 eV). The condition, in a one-electron description, at which axial ligand splitting from an octahedron (see Figure S11) is met is when the $3d_{z^2}$ and $3d_{xy}$ orbitals have degenerate energies (10Dq = 2.24 eV and Ds = 0.56 eV).

5 Some broadening contributions that (do not) affect the RIXS relative intensity profiles

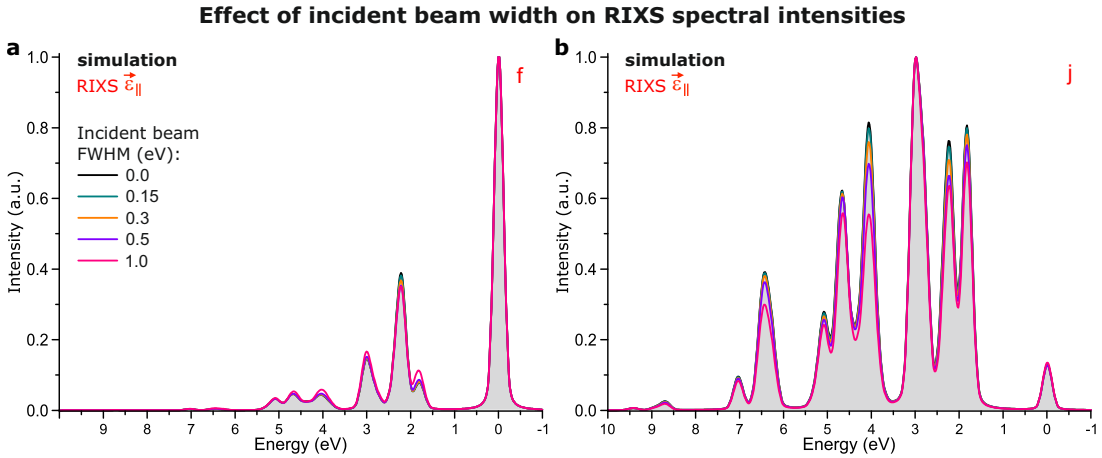

Figure S12: Effect of the FWHM of the incoming beam on the relative peak intensities of two randomly selected depolarized RIXS spectra, ***f*** in (a) and ***j*** in (b). The modifications are a result of weighting in spectra at all excitation energies around the selected energy, following a Gaussian distribution with the indicated FWHM. The gray areas under the black solid lines highlight the case of an infinitely sharp incoming beam (FWHM is 0 eV). The legend in (a) applies equally to (b).

Figure S12 shows the effect of the energy width of the incident beam on the intensities of the RIXS spectra. Simulations for depolarized RIXS spectra are shown, but the result is identical for the polarized case. RIXS spectra at two energies are given as examples. The simulations assume an incoming X-ray beam with a Gaussian energy distribution which excite at several excitation energies simultaneously as a result of the energy distribution. All excited states are summed according to the weight of the Gaussian at each energy. Different widths of the incoming beam are compared. At excitation energy ***f***, Figure S12a, there is almost no change in relative peak intensities up to a 0.5 eV FWHM. For energy ***j***, Figure S12b, there is only little change in relative intensities within the RIXS spectrum up to this incoming beam width. Only when the FWHM of the Gaussian exceeds 0.5 eV, relatively large modifications of the observed RIXS spectrum are expected.

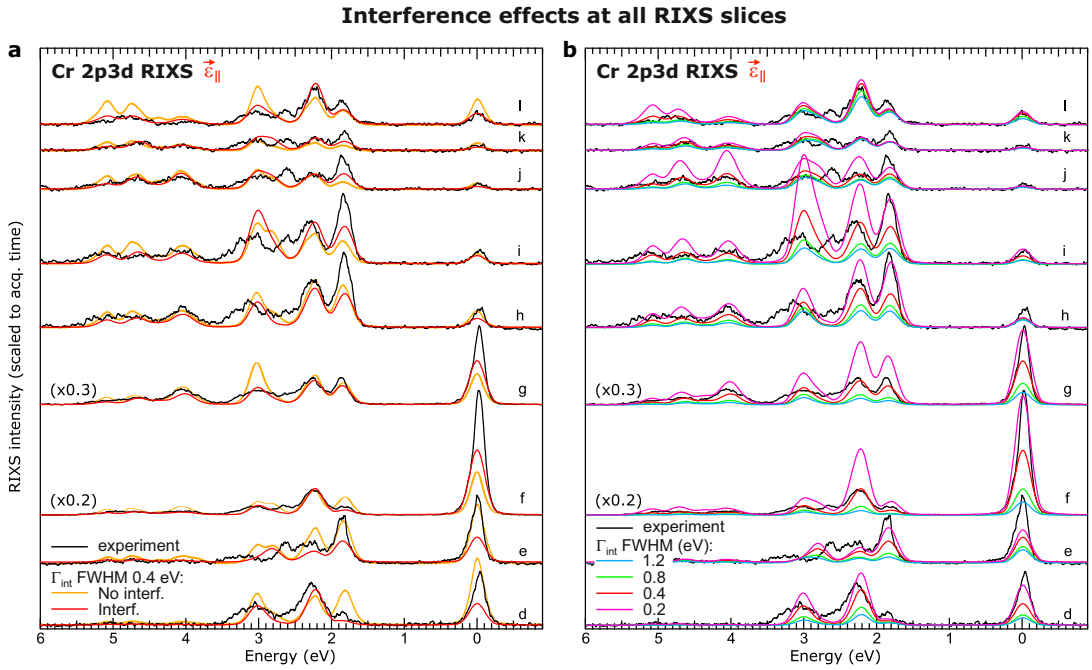

Figure S13: (a) Experimental depolarized RIXS spectra at excitation energies ***d*** - ***l*** (black lines), together with corresponding calculations with a Lorentzian broadening FWHM of 0.4 eV, with (red lines) and without (orange lines) RIXS interference. (b) Experimental depolarized RIXS spectra at excitation energies ***d*** - ***l*** (black lines), together with corresponding calculations with varying Lorentzian broadenings.

Figure S13 shows the effect of interference and the related lifetime of the core-hole excited state (the RIXS intermediate state) on the relative intensity profile of RIXS spectra. In Figure S13a, the Lorentzian broadening of the RIXS intermediate state is set to 0.4 eV FWHM. Subsequently, the RIXS spectra of ruby at several excitation energies are calculated following the Kramers-Heisenberg equation that describes the RIXS process. The results are compared to calculations in which the X-ray absorption and emission steps of the process are performed independently and subsequently, without interfering with each other. The effect of RIXS interference processes on the spectral RIXS intensities becomes clear by combing the two calculations. It is for example observed that the relative intensities of the spectra at excitation energies ***d*** - ***f*** are strongly influenced by the interference effects. Also, 3d states with higher energies are suppressed by RIXS interference processes. The extent to which RIXS interference plays a role in alternating RIXS intensities depends on the Lorentzian broadening of the intermediate state. The larger the Lorentzian broadening, the larger the interference effect will be.[S6,S7] Different values of this broadening will thus result in different relative intensities of the RIXS spectral features. This is illustrated in Figure S13b. In this respect, note that it is common to simulate the L_2 edge of XAS spectra with a larger Lorentzian broadening than the L_3 edge. This results from the additional (super) Coster-Kronig decay paths at the L_2 edge, leading to a shorter core-hole excited life time.[S6] Through careful comparison with our experiment we find in a similar way that applying Lorentzian broadenings of 0.2, 0.4 and 1.2 eV FWHM yield the best simulations for energies up to 577.5 eV, between 577.5-584 eV, and above 584 eV, respectively.

6 Derivation of polarization-dependent optical and RIXS selection rules

In this part, we discuss the polarization dependence of 2p3d RIXS transition intensities for Cr^{3+} following the derivation made by Matsubara et al.[S5] and compare them to optical absorption. Dichroism is a property of the space group of the crystal[S8,S9] and not of the point group of the absorbing site. However, because the main axis of the trigonal point group of the Cr impurity in ruby is collinear to the main axis of the trigonal space group of the corundum hexagonal cell, we will describe the derivation using the irreducible representation of the point group of the Cr site used for the CFM calculations. The derivation of the selection rules results from the determination of the conditions on the initial and final states of a transition, for which the transition matrix element (the square root of the intensity) is non-zero. According to the Wigner-Eckart theorem, the transitions matrix element between $|\alpha\Gamma\gamma\rangle$ and $|\alpha'\Gamma'\gamma'\rangle$ is proportional to the Clebsch-Gordan coefficient:

$$\langle\alpha\Gamma\gamma|T_q^{(k)}|\alpha'\Gamma'\gamma'\rangle \propto \langle\Gamma'\gamma' kq|\Gamma\gamma\rangle \tag{1}$$

where Γ, Γ' are irreducible representations from the group; γ, γ' are the basis of the group; and α, α' are quantum numbers. $T_q^{(k)}$ is the q-th component of the spherical tensor operator $T^{(k)}$ of rank k. Here T is the electric dipole transition operator. We first recall the selection rules in O_h point group and then provide the derivation of the selection rules in C_{3v} and C_3 point groups to discuss to what extent the selection rules are affected by the choice of the point group for the crystal field of Cr^{3+} in corundum. The branching between the irreducible representations is given in Table S2. This corresponds to the case of a single crystal sample. Then we consider the case of an isotropic sample i.e. a powder as studied in this work. We first neglect the spin-orbit interaction. We will discuss its effect and the

effect of the interferences in the intermediate state of the RIXS process in a third part.

Table S1: Branching of the irreducible representations of 3d states.

O_h		C_{3v}		C_3
A_{1g}	$\rightarrow$	A_1	$\rightarrow$	A
A_{2g}	$\rightarrow$	A_2	$\rightarrow$	A
E_g	$\rightarrow$	E	$\rightarrow$	^{1}E $\oplus^2$E
T_{1g}	$\rightarrow$	$A_2\oplus$ E	$\rightarrow$	A $\oplus^1$E $\oplus^2$E
T_{2g}	$\rightarrow$	$A_1\oplus$ E	$\rightarrow$	A $\oplus^1$E $\oplus^2$E

Table S2: Light polarization (electric dipole transition operator).

Electric dipole	O_h	C_{3v}	C_3
Parallel (z)	T_{1u}	A_1	A
Perpendicular (x, y)	T_{1u}	E	^{1}E $\oplus^2$E

6.1 Single crystal case

Following and using the same conventions as Matsubara et al.,[S5] we chose the (x, y, z) axes such that the incident light propagates along x and the incident polarization is in the (y, z) plane. The emitted light propagates in the z direction and the emitted polarization, which we do not distinguish, is in the (x, y) plane. Thus y is normal to the scattering plane (x, z). With these conventions, in O_h, in depolarized configuration the incident polarization is described by the z basis of the T_{1u} irreducible representation. In the polarized configuration, the incident polarization is described by the y basis of T_{1u}. Then, the emitted polarization is

described by the x and y basis of T_{1u}. This yields the following selection rules:

$$\text{depolarized} \tag{2}$$

$$\sum_{\gamma=x,y} A_{2g} \otimes T_{1u,z} \otimes T_{1u,\gamma} = T_{1g} \oplus T_{2g},$$

$$\text{polarized} \tag{3}$$

$$\sum_{\gamma=x,y} A_{2g} \otimes T_{1u,y} \otimes T_{1u,\gamma} = A_{2g} \oplus E_g \oplus T_{1g} \oplus T_{2g}.$$

In C_{3v} symmetry, the incident polarization has A_1 (z) symmetry in depolarized configuration and E (y) symmetry in the polarized configuration (see Table S2), yielding:

$$\text{depolarized} \tag{4}$$

$$A_2 \otimes A_1 \otimes E = E,$$

$$\text{polarized} \tag{5}$$

$$A_2 \otimes E \otimes E = A_1 \oplus A_2 \oplus E.$$

This means that in the depolarized case only states of symmetry E can be reached via the RIXS process. In C_3, the selection rules become:

$$\text{depolarized} \tag{6}$$

$$\sum_{\gamma=1,2} A \otimes A \otimes {}^{\gamma}E = {}^{1}E \oplus {}^{2}E,$$

$$\text{polarized} \tag{7}$$

$$\sum_{\gamma=1,2} A \otimes {}^{2}E \otimes {}^{\gamma}E = A \oplus {}^{2}E.$$

Thus also in C_3 symmetry one should obtain a polarization dependence of the dd-excitations in 2p3d RIXS. Altogether, we see that both in C_{3v} and C_3 symmetries, the intensity of the elastic line (RIXS transition from A (A_2) to A (A_2) irreducible representations in C_3 (C_{3v})) is predicted to be zero in the depolarized configuration and non-zero in the

polarized configuration. The polarization dependence of the optical absorption corresponds to only the first step in the descriptions used above. Published polarized light data of single crystals correspond to: i) the incident light being parallel to the main axis of the crystal (here the trigonal axis, which is parallel to the c-axis in Figure 1, which is parallel to the z axis of the Cr site) and ii) the incident light being perpendicular to the main axis of the crystal (etcetera). The selection rules for optics and RIXS are summarized and compared for the C_3 point group in Table S3.

Table S3: Selection rules without spin-orbit coupling from Cr^{3+} ground state A_2 (C_{3v}) and A (C_3).

C_{3v}	Incident light polarization	
	A_1	E
Final state OAS	A_2	E
Final state 2p3d RIXS	polarized: $A_1 \oplus A_2 \oplus E$	depolarized: E
C_3	Incident light polarization	
	A	$^1E \oplus ^2E$
Final state OAS	A	$^1E \oplus ^2E$
Final state 2p3d RIXS	polarized: A $\oplus ^1E$	depolarized: $^1E \oplus ^2E$

6.2 Isotropic sample case

As a first approximation in C_{3v}, we describe the case of an isotropic sample by considering the three cases arising from circular permutation of x, y and z in equation (3):

$$\sum_{(\Gamma,\Gamma')=(A_1,E),\Gamma\neq\Gamma} A_2 \otimes \Gamma \otimes \Gamma' = 2E, \quad \text{depolarized} \tag{8}$$

$$\sum_{(\Gamma,\Gamma')=(A_1,E),\Gamma=\Gamma} A_2 \otimes \Gamma \otimes \Gamma' = A_1 \oplus 2A_2 \oplus E, \quad \text{polarized} \tag{9}$$

In C_3, one obtains:

$$\sum_{(\Gamma,\Gamma')=(A_1,{}^iE),\Gamma\neq\Gamma} A \otimes \Gamma \otimes \Gamma' = 2({}^1E \oplus {}^2E), \quad \text{depolarized} \tag{10}$$

$$\sum_{(\Gamma,\Gamma')=(A_1,{}^iE),\Gamma=\Gamma} A \otimes \Gamma \otimes \Gamma' = 3A \oplus {}^1E \oplus {}^2E, \quad \text{polarized} \tag{11}$$

Altogether, this demonstrates that polarization dependence is expected for 2p3d RIXS, even for an isotropic sample, contrary to optical absorption spectroscopy.

6.3 Effect of the spin-orbit coupling and interferences in the intermediate state

If spin-orbit coupling is included, then momentum transfer between spin and orbit is possible and the selection rules derived above are relaxed. In that case, the RIXS intensity of the elastic line is dominated by the number of channels. In the polarized configuration there are more channels available than in the depolarized configuration. Moreover, interferences due to the life time of the intermediate state increases the number of possibilities for resonant decay emission channels. Again, because no momentum change is necessary in the polarized configuration, the RIXS intensity is stronger than in the depolarized case.

References

(S1) Tanabe, Y.; Sugano, S. On the absorption spectra of complex ions. I. *J. Phys. Soc. Jpn.* **1954**, *9*, 753–766.

(S2) Fairbank Jr, W. M.; Klauminzer, G. K.; Schawlow, A. L. Excited-state absorption in ruby, emerald, and MgO:Cr^{3+}. *Phys. Rev. B* **1975**, *11*, 60.

(S3) McClure, D. S. Optical spectra of transition- metal ions in corundum. *J. Chem. Phys.* **1962**, *36*, 2757–2779.

(S4) Macfarlane, R. M. Analysis of the spectrum of d^3 ions in trigonal crystal fields. *J. Chem. Phys.* **1963**, *39*, 3118.

(S5) Matsubara, M.; Uozumi, T.; Kotani, A.; Harada, Y.; Shin, S. Polarization dependence of resonant X-ray emission spectra in $3d^n$ transition metal compounds with n = 0, 1, 2, 3. *J. Phys. Soc. Jpn.* **2002**, *71*, 347–356.

(S6) de Groot, F. M. F.; Kotani, A. *Core level spectroscopy of solids*; CRC Press: Boca Raton, Etats-Unis, 2008.

(S7) Kramers, H. A.; Heisenberg, W. Über die Streuung von Strahlung durch Atome. *Z. Phys.* **1925**, *31*, 681–708.

(S8) Juhin, A.; Brouder, C.; Arrio, M.-A.; Cabaret, D.; Sainctavit, P.; Balan, E.; Bordage, A.; Seitsonen, A.; Calas, G.; Eeckhout, S.; Glatzel, P. X-ray linear dichroism in cubic compounds: The case of Cr^{3+} in $MgAl_2O_4$. *Phys. Rev. B* **2008**, *78*, 195103.

(S9) Brouder, C. Angular dependence of X-ray absorption spectra. *J. Phys.: Condens. Matter* **1990**, *2*, 701.